JASA ARTICLE

Optical phase contrast imaging for absolute, quantitative measurements of ultrasonic fields with frequencies up to 20 MHz

Aaron M. Goldfain,[a] Christopher S. Yung,[b] Kimberly A. Briggman,[c] and Jeeseong Hwang[d]
Applied Physics Division, National Institute of Standards and Technology, Boulder, Colorado 80305, USA

ABSTRACT:
The technique of phase contrast imaging, combined with tomographic reconstructions, can rapidly measure ultrasonic fields propagating in water, including ultrasonic fields with complex wavefront shapes, which are difficult to characterize with standard hydrophone measurements. Furthermore, the technique can measure the absolute pressure amplitudes of ultrasonic fields without requiring a pressure calibration. Absolute pressure measurements have been previously demonstrated using optical imaging methods for ultrasonic frequencies below 2.5 MHz. The present work demonstrates that phase contrast imaging can accurately measure ultrasonic fields with frequencies up to 20 MHz and pressure amplitudes near 10 kPa. Accurate measurements at high ultrasonic frequencies are performed by tailoring the measurement conditions to limit optical diffraction as guided by a simple dimensionless parameter. In some situations, differences between high frequency measurements made with the phase contrast method and a calibrated hydrophone become apparent, and the reasons for these differences are discussed. Extending optical imaging measurements to high ultrasonic frequencies could facilitate quantitative applications of ultrasound measurements in nondestructive testing and medical therapeutics and diagnostics such as photoacoustic imaging. https://doi.org/10.1121/10.0005431

(Received 22 January 2021; revised 19 May 2021; accepted 3 June 2021; published online 29 June 2021)
[Editor: Keith A. Wear] Pages: 4620–4629

I. INTRODUCTION

Quantitative measurements of ultrasonic fields in water are critical to a variety of applications, including nondestructive testing, as well as medical imaging and therapeutics, including ultrasound and photoacoustic imaging, and ultrasonic tissue ablation. The most common method for measuring an ultrasonic pressure field is scanning a small receive area, calibrated, piezoelectric or fiber optic hydrophone throughout the field to collect the pressure vs time curves at many points as described in the International Electrotechnical Commission's (IEC) standards 62127-1 and 62127-3.[1–3] The hydrophone is typically calibrated either by a primary measurement in a metrology institute or through a secondary comparison to a previously calibrated hydrophone as described in IEC 62127-2.[1,4–6] The most widely used primary calibration method for the 1–20 MHz frequency range is based on optical interferometric measurements of the displacement of a thin pellicle caused by a planar ultrasonic wave.[7–12] The reciprocity method also has been demonstrated as a primary calibration method at frequencies up to 15 MHz,[13,14] and time delay spectrometry, a relative calibration procedure, can be used to extend an absolute calibration to additional frequencies.[15]

Although effective for many applications, scanning a calibrated hydrophone to measure a three-dimensional (3D) ultrasonic field has numerous limitations, especially when measuring ultrasonic fields generated during photoacoustic imaging. Hydrophone scanning is slow as a result of the mechanical movement of the hydrophone, it can perturb the field being measured, it requires the measurement conditions (temperature, water purity, etc.) to match those under which the primary calibration of the hydrophone was performed, and the pressure wavefront's shape must match the shape of the hydrophone surface.[1,2,16] Commercially available calibrated hydrophones typically have flat-end active elements at the sensing end or aperture and the calibration is performed with plane wave ultrasonic fields, therefore, the wavefronts of the pressure field being evaluated must be normal to and planar across the sensing aperture for the best accuracy. If deviations from the planarity are comparable to or larger than the ultrasonic wavelength, the measurement accuracy is compromised because the hydrophone's output is typically sensitive to only the average integrated pressure across its active element.[17,18] Frequency-dependent correction factors, which account for this spatial averaging effect, can restore the measurement accuracy,[2,3,5,17–20] but obtaining the correction factors increases the measurement burden and requires assumptions or prior knowledge of the ultrasonic field's shape. Smaller aperture hydrophones are less susceptible to spatial averaging errors,[2,3] but they have significantly lower sensitivities. Thus, hydrophone scanning is difficult to apply to ultrasonic fields generated during photoacoustic imaging, which can have ultrasonic frequencies from a few MHz to over 100 MHz,[16] have varying wavefront shapes due to the complex structures of the tissues where the waves originate[21,22] and have relatively low-pressure amplitudes (typically below 10 kPa).[23]

a)ORCID: 0000-0002-4119-3983.
b)ORCID: 0000-0002-7912-6591.
c)ORCID: 0000-0001-8341-998X.
d)Electronic mail: jeeseong.hwang@nist.gov, ORCID: 0000-0002-9801-8529.

A wide range of novel optical methods are being explored to characterize spatially complex ultrasonic fields with high frequencies and lower pressures. These methods have been reviewed in detail elsewhere[16,24] and can be broadly categorized as free-space optical imaging methods, which are sensitive to the refractive index (RI) change that an ultrasonic field induces in the propagating medium,[21,25–30] methods that measure changes in an optical resonator due to the ultrasonic field,[31–33] and methods that measure displacements or RI changes at the surface of the ultrasound propagating media.[34–36] Similar to measurements with piezoelectric or fiber optic hydrophones, optical resonator methods and surface-based methods rely on having the sensing element or surface within the ultrasonic field, which can disturb the field being measured.

Free-space optical imaging methods, on the other hand, are particularly well suited for characterizing ultrasonic fields with spatially complex wavefronts. Optical imaging methods can be 10–100 times faster than hydrophone scanning methods, they do not perturb the pressure field because they do not involve a physical ultrasound sensor, and can measure pressure wavefronts of arbitrary shapes.[16,25,26,37,38] Optical imaging methods exploit the piezo-optic effect, wherein the local RI of the ultrasound propagating media (typically water) changes in response to the propagating ultrasonic pressure, which, in turn, induces a phase shift in the light that traverses the ultrasonic field. The methods involve measuring the change in the phase of a light wave that traverses the propagating ultrasonic pressure field and performing a tomographic reconstruction to determine the 3D pressure distribution.[16,26] Many related phase measurement schemes have been reported, including (but not limited to) schlieren imaging,[27,39] optical shadowgraphy,[28] laser doppler vibrometry,[29] and quantitative phase contrast imaging.[25,30] In principle, all of these techniques can measure the absolute pressure amplitudes if the piezo-optic coefficient of the media and wavelength of the light are known. However, because of practical difficulties, without comparison to an absolute pressure calibration measurement, these techniques often produce only a measurement of the relative pressure amplitudes.[27,29,39,40] To our knowledge, measurements of absolute pressure amplitudes have not been demonstrated with optical imaging methods for ultrasonic frequencies above 2.5 MHz.[25,28,30,37]

The measurement accuracy of the optical imaging of ultrasound can be compromised at high ultrasonic frequencies when light diffraction by the ultrasonic field becomes significant. A simple dimensionless parameter, the Klein-Cook parameter,[41,42] describes when diffraction effects are significant and may be used as a metric to understand and modify the experimental conditions to improve the measurement accuracy at high frequencies. By comparing optical phase contrast measurements of ultrasonic fields to measurements made with a calibrated hydrophone, this paper demonstrates that phase contrast imaging can accurately measure ultrasonic fields with frequencies up to 20 MHz. Phase contrast imaging could serve to quickly and quantitatively characterize spatially complex ultrasonic fields with high frequencies such as those generated in nondestructive testing,[43] ultrasound imaging,[44] or photoacoustic imaging.[16,21,23,45] In these imaging applications, the high-resolution spatial information provided by the phase contrast imaging can improve the reconstructed image quality.[22] Although it is not the focus of the present work, phase contrast imaging might also be developed as a primary calibration method for hydrophones and transducers.

II. METHODS

A. Measurement concept

A pressure field propagating in a medium can be optically imaged because a local change in the RI of the pressure-induced medium modifies the phase of the transmitted light. The pressure-induced local RI change is $\Delta n = \Delta P C_p$, where ΔP is the difference between the induced and ambient pressure and C_p is the piezo-optic coefficient.[26] For small pressure amplitudes (<10 MPa in water), C_p is approximately constant.[46] When a collimated optical beam (vacuum wavelength λ) passes through an ultrasonic pressure field, assuming light diffraction effects are negligible, the intensity of the optical beam transmitted through the pressure field remains unchanged. However, the transmitted light acquires a spatially varying phase shift

$$\varphi(y,z) = \frac{2\pi C_p}{\lambda}\int \Delta P(x,y,z)dx, \tag{1}$$

where the integral is in the direction of light propagation.[16,26] This instantaneous phase shift can be measured with quantitative phase contrast imaging, and a tomographic reconstruction (Sec. II D) can invert the pressure integral to determine the 3D distribution of the pressure field.

Both Eq. (1) and the tomographic reconstruction step assume light traverses straight through the ultrasonic field with negligible optical diffraction effects. In this case, the light field acquires only a phase shift and little amplitude variation.[41] The problem of light diffraction by ultrasound has been studied in detail. For sinusoidal, planar ultrasonic fields of frequency f and amplitude $\Delta P_{\max}$, the optical amplitude variations remain small if both the Raman-Nath parameter[42] (the maximum phase shift), $\nu = 2\pi C_p L \Delta P_{\max}/\lambda \ll 1$, and the Klein-Cook parameter,[41,42]

$$Q = \frac{2\pi\lambda L f^2}{nc^2} \leq 2, \tag{2}$$

where L is the extent of the ultrasonic field in the light's propagation direction, n is the RI of the undisturbed medium, and c is the speed of sound. Thus, diffraction effects are more significant at higher pressure amplitudes, at higher ultrasonic frequencies, and for ultrasonic fields with a larger spatial extent. In this work, light diffraction effects are limited by maintaining the experimental conditions such that $\nu \leq 0.05$ (largest measured phase shift) and $Q \leq 2.4$ ($\lambda = 470$ nm, $L = 6$ mm, $f = 20$ MHz in water) as detailed below in Sec. III.

B. Phase contrast apparatus

A custom-built quantitative phase contrast imaging system is used to measure the spatially varying phase shift that light acquires on traversing a pressure field generated by an ultrasonic transducer. Although many other optical imaging methods can measure the phase shift of light,[16,26] here, a quantitative phase contrast imaging approach is used because it is inherently capable of wide-field phase imaging, involves simple image postprocessing steps, and allows the imaging system to be focused at the center of the ultrasonic field, which helps to minimize optical diffraction effects.[28] Phase contrast imaging requires a few repeated measurements of the same ultrasonic field in which different optical filters are placed in the imaging path, but this is not usually a significant limitation when the same ultrasonic fields can be repeatedly generated. Phase contrast imaging also requires the ultrasound propagating media (typically water) to be free from small particulates because particles in the light path can scatter light and appear as noise in the recorded images.

Figure 1(A) is a schematic of the quantitative phase contrast imaging system, which is based on the concept from Refs. 25 and 30. Strobed illumination by a pulsed diode laser (470 nm, 130 ps, 80 mW peak power; Hamamatsu PLP10-047, Bridgewater, NJ, USA), synchronized with the ultrasound generation, captures a snapshot of the instantaneous ultrasonic field. The laser light is spatially filtered through a single-mode optical fiber (Thorlabs 460HP, Newton, NJ, USA) and collimated into a wide-field illumination beam

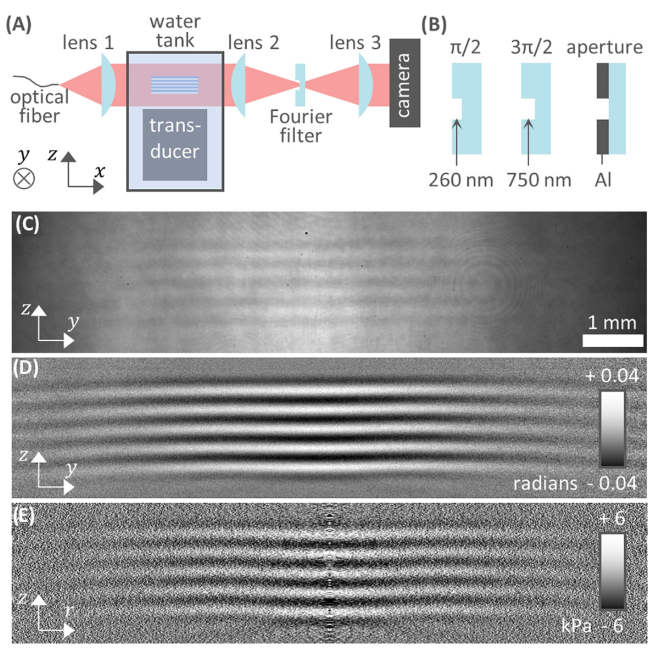

FIG. 1. (Color online) (A) A top view of the phase contrast imaging apparatus and coordinate system (bottom left). (B) Cross-sectional cartoons of the circular Fourier filters. [(C)–(E)] Images of a planar, 5 MHz, 5-cycle, tone burst pressure field. (C) The raw camera image with the $\pi/2$ Fourier filter. (D) The calculated phase shift image. Note that the y axis coordinate is into-the-page in the schematic in (A). (E) The reconstructed axisymmetric pressure distribution. The horizontal direction is the radial direction, r, in the axisymmetric reconstruction with the axis of symmetry (AOS) in the center of the image. The scale bar in (C) applies to (D) and (E) as well.

with lens 1 (Thorlabs AC254-075-A-ML). A 4f system[47] (lens 2 and 3; Thorlabs AC508-250-A-ML and AC508-150-A-ML) focused in the center of the ultrasonic field relays the image through a Fourier filter and to a camera (Mightex MCE-B013-UW, Pleasanton, CA, USA). The pixel size in the image corresponds to $8.74\,\mu\text{m} \times 8.74\,\mu\text{m}$ as calibrated with a 1951 USAF target (Edmund Optics DA007E, Barrington, NJ, USA), and the total field of view of the image is $11.2\,\text{mm} \times 8.95\,\text{mm}$ (1280 pixels × 1024 pixels), which is large enough to capture the entire extent of the measured ultrasonic fields. Portions of the water tank are lined with 0.5 in. thick, angled polyurethane (McMaster-Carr 8716K66, Elmhurst, IL, USA) such that ultrasound reflections from the inner wall of the aluminum water tank are attenuated and do not reenter the detection volume.

Three separate images are acquired, each with different Fourier filters [termed the "$\pi/2$," "$3\pi/2$," and "aperture" filters; Fig. 1(B)], to calculate the acquired phase shift. The filters modify the zero-order Fourier component of the image differently than the rest of the image. The $\pi/2$ and $3\pi/2$ filters are 1 in. in diameter, fused silica optical flats (ThorlabsWG41010, Newton, NJ, USA) with a $100\,\mu$m diameter and optically flat recesses on one side (260-nm and 750-nm depths, respectively). The recesses are fabricated using a fluoroform and argon reactive ion dry etch. Illumination through the 260 ± 10 nm deep or 750 ± 10 nm deep recesses (as measured with a Tencor to KLA Tencor. Milpitas, CA, USA) results in phase shifts of the zero-order beam by $\pi/2$ or $3\pi/2$, respectively. The aperture filter is an optical flat with 100 nm of aluminum magnetron sputter coated everywhere except over a $100\,\mu$m diameter circle in the center of the flat.

C. Imaging ultrasonic fields

In this paper, a variety of ultrasonic fields generated by different types of piezoelectric transducers with varying waveforms and frequencies are investigated. The waveforms include 2–20 MHz sinusoidal tone bursts with both planar and curved wavefronts and a broadband pulse with a planar wavefront. A 5 MHz, 6 mm diameter flat transducer (Olympus V310-SU, Waltham, MA USA) is used for planar tone bursts with frequencies of 2–5 MHz as well as for the broadband pulse; a 50 MHz, 6 mm diameter flat transducer (Olympus V358-SU) for planar tone bursts with frequencies of 7.5–20 MHz; a 5 MHz, 25 mm diameter focused transducer (CTS Valpey IL0506HR, 19 mm focal length, Hopkinton, MA, USA) for curved tone bursts with frequencies of 2–5 MHz; and a 50 MHz, 6 mm diameter focused transducer (Olympus V390-SU/RM, 13 mm focal length) for curved tone bursts with frequencies of 7.5–20 MHz. For the tone bursts, driving voltages of 1–5 V peak-to-peak are used with the lower voltages being used near the resonant frequencies of the transducers to keep the peak pressure amplitudes similar at each frequency and well below the 100- kPa damage threshold for the hydrophone (described in Sec. II E) used to detect the ultrasonic fields. The broadband electronic pulse is approximately Gaussian shaped with a voltage amplitude of 120 V and a full width at half-maximum of 4 ns. As seen in Sec. III, the peak ultrasonic pressure amplitudes are a few kPa for planar waves and tens of kPa for the focused waves. This pressure range is typical for photoacoustic imaging[23] but significantly smaller than the few MPa pressures used in medical ultrasonic imaging.[2] Because the pressure amplitudes are relatively small and all ultrasound measurements are made within 28 mm of the transducer's active element, the nonlinear propagation parameter (also called the local distortion parameter) is kept below 0.1, and the nonlinear propagation effects are not expected to be significant.[2]

To image the ultrasonic pulses, the laser pulse illumination and ultrasonic pulse generation are synchronized with a function generator (Tektronix AFG3252, Beaverton, OR, USA). For the tone bursts, the electronic burst train is generated with the same function generator, and for the broadband pulse, the pulse train is generated with an ultrasonic pulser/receiver (energy setting 1, damping setting 0; Panametrics 5601 A/TT, Waltham, MA, USA). To account for the time that the ultrasound takes to travel from the transducer into the imaging field of view, the laser pulse generation is delayed relative to the ultrasound generation. For the tone bursts, a burst repetition rate of 125 kHz with a camera exposure time of 345 ms is used, and for the broadband pulse, a burst repetition rate of 10 kHz with a camera exposure time of 750 ms is used. Therefore, each image with a Fourier filter is the sum of multiple snapshots with many identical pulses for an improved signal-to-noise ratio. A more energetic laser and a more sensitive camera would facilitate fewer pulses per exposure time. All data are recorded with the water bath at 23 °C as measured with an electronic thermometer (ThermoWorks Thermamite 5, American Fork, UT, USA) placed near the ultrasonic transducer.

To calculate the optical phase shift image (see Sec. II D), five images are recorded for each ultrasonic field: $I_{+,\mathrm{on}}$ and $I_{+,\mathrm{off}}$ with the $\pi/2$ filter installed and the transducer on and off; $I_{-,\mathrm{on}}$ and $I_{-,\mathrm{off}}$ with the $3\pi/2$ filter installed and the transducer on and off; and I_{zero} with the aperture filter installed and the transducer on. Each image represents the average of 10 consecutive frames for the tone bursts or 100 frames for the broadband pulse, which effectively reduces camera shot noise and noise resulting from occasional stray dust particles in the water bath. The broadband pulse requires more frames to reduce the shot noise because of the lower number of pulses per image exposure time. Last, a dark image (average of 300 frames) recorded with no illumination is subtracted from each image. The measurement procedure requires about 10 min for the tone bursts and 15 min for the broadband pulse, including about 5 min to manually change and align the Fourier filters. Although not implemented here, a more energetic light source and automated filter wheel or liquid crystal spatial light modulator could significantly reduce the measurement time.

D. Pressure distribution reconstruction

The optical phase shift is calculated from the five recorded images in the same manner as in Refs. 25 and 30. The initial electric field, $\boldsymbol{E_0}$, after transmission through the ultrasonic field becomes $\boldsymbol{E} = \boldsymbol{E_0} e^{i\varphi} = \boldsymbol{E_0} e^{i\varphi} - \boldsymbol{\alpha} + \boldsymbol{\alpha}$, where $\boldsymbol{\alpha}$ is the zero-order component of the electric field that the phase filter modifies, and $\boldsymbol{E}_0 e^{i\varphi} - \boldsymbol{\alpha}$ is the rest of the field. Thus, the transmitted intensities are $\boldsymbol{I}_{+,\mathbf{on}} = |\boldsymbol{E}_0 e^{i\varphi} - \boldsymbol{\alpha} + \boldsymbol{\alpha} e^{i\pi/2}|^2$, $\boldsymbol{I}_{-,\mathbf{on}} = |\boldsymbol{E_0} e^{i\varphi} - \boldsymbol{\alpha} + \boldsymbol{\alpha} e^{i3\pi/2}|^2$, $\boldsymbol{I}_{\mathbf{zero}} = |\boldsymbol{\alpha}|^2$, acquired with the $\pi/2$ filter, $3\pi/2$ filter, and aperture filter, respectively. If no sound field is present (the transducer is off), the recorded intensities with the $\pi/2$ and $3\pi/2$ filters are $\boldsymbol{I}_{+,\mathbf{off}} = |\boldsymbol{E_0}|^2$ and $\boldsymbol{I}_{-,\mathbf{off}} = |\boldsymbol{E_0}|^2$, respectively. These equations can be solved for the phase shift, yielding

$$\sin\varphi = \frac{(I_{+,\mathrm{on}} - I_{+,\mathrm{off}}) - (I_{-,\mathrm{on}} - I_{-,\mathrm{off}})}{4E'_{\mathbf{0}}\sqrt{I_{\mathrm{zero}}}} \tag{3}$$

and

$$\cos\varphi = \frac{\sqrt{I_{\mathrm{zero}}}}{E'_{\mathbf{0}}} - \frac{(I_{+,\mathrm{on}} - I_{+,\mathrm{off}}) - (I_{-,\mathrm{on}} - I_{-,\mathrm{off}})}{4E'_{\mathbf{0}}\sqrt{I_{\mathrm{zero}}}}, \tag{4}$$

where $E'_0 = \sqrt{(I_{+,\mathrm{off}} + I_{-,\mathrm{off}})/2}$. The inverse tangent operation determines φ from Eqs. (3) and (4).

Because the ultrasonic fields imaged are axisymmetric, a tomographic reconstruction is performed by applying the inverse Abel transform[48] to a single phase image. The inverse Abel transform is applied with the Python package PyAbel[49] using the BASEX method[50] and a regularization parameter of 1000. Smaller values for the regularization parameter lead to more noise near the axis of symmetry (AOS), but if the parameter is made too large, the reconstructed pressure amplitude begins to decrease near the AOS.[49,50] The value of $C_P = (1.43 \pm 0.06) \times 10^{-10}\,\mathrm{Pa}^{-1}$ is used based on Ref. 51 for 470 nm light in pure water at 23 °C. Whereas the measurements here are of axisymmetric pressure fields, non-axisymmetric fields could be measured by capturing multiple phase contrast images after rotating the ultrasonic source and using the inverse Radon transform to perform the tomographic reconstruction.[21,25,30]

E. Hydrophone comparison

The local pressure amplitudes in the reconstructed pressure fields are compared to separate measurements with a commercial calibrated hydrophone (HNP-1000, Onda Corporation. Sunnyvale, CA, USA), which has a 1 mm diameter aperture. For the hydrophone measurement, the hydrophone is oriented perpendicular to the ultrasonic wavefronts and kept in the $\boldsymbol{y}$-$\boldsymbol{z}$ plane, which intersects the transducer's AOS [see the coordinate definitions in Fig. 1(A)]. The ultrasonic field is measured at different locations in the $\boldsymbol{y}$-$\boldsymbol{z}$ plane within the field of view of the imaging system. The hydrophone measurement location within the field of view is determined by recording an image of the hydrophone aperture with the phase imaging camera. The voltage vs time signals are digitized with a memory waveform digitizer (Alazar Technologies ATS9350-102, Pointe Claire, Quebec, Canada). A preamp (Onda Technologies AH-2010-100) and direct current (DC) block filter (Onda Technologies BNP) are used between the hydrophone and digitizer. To reduce random noise, 100 repeated measurements are averaged. The manufacturer (Onda Technologies) of the hydrophone and preamplifier provides a frequency-dependent voltage-to-pressure amplitude calibration [traceable to the National Physical Laboratory (NPL) in the United Kingdom] for the hydrophone and preamplifier combination, which is nominally 2000 nV/Pa but varies slightly with the frequency. The provided uncertainty in the calibration is 11% for ultrasonic frequencies from 1 MHz up to (but not including) 15 MHz and 16% for frequencies of 15–20 MHz. According to the manufacturer, the hydrophone was calibrated through a comparison to a reference hydrophone provided by NPL, and the uncertainty in the calibration is mainly due to systematic uncertainties in the reference hydrophone's calibration.

III. RESULTS AND DISCUSSION

Sinusoidal tone bursts and a broadband pulse generated from flat ultrasonic transducers (Fig. 2) are first examined. The calibrated hydrophone is used to record the pressure vs time curves at various locations in the y-z plane, and for each measurement location, the position of the hydrophone aperture is determined by recording an image of it with the phase contrast camera. Then, phase contrast images of the ultrasonic field with no hydrophone are recorded. The ultrasound measurement locations are approximately 25 mm from the face of the transducer. A pressure vs time curve is obtained from the phase contrast measurements by calculating the average pressure across the area corresponding to the hydrophone's geometric aperture in each x-y plane of the reconstructed pressure distribution. Spatial averaging of the phase contrast measurement across the hydrophone's aperture mimics the hydrophone response, which is expected to be proportional to the average pressure across the hydrophone aperture.[2,17,18] The effective and geometrical apertures of the hydrophone are assumed equivalent, which is justified by previous studies of needle polyvinylidene fluoride hydrophones given that $\pi f D/c > 4$ in the present measurement conditions, where D is the

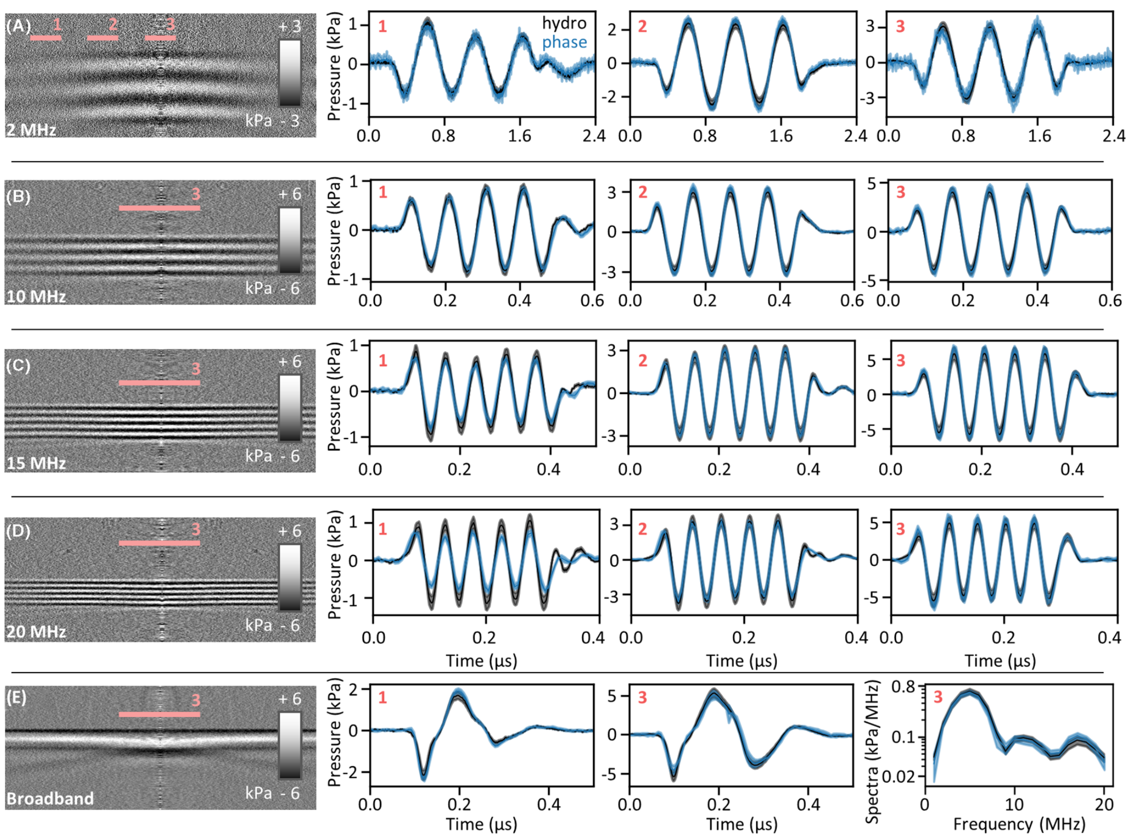

FIG. 2. (Color online) Pressure fields generated from flat ultrasonic transducers. [(A)–(D)] 2 MHz, 10 MHz, 15 MHz, and 20 MHz tone bursts. (E) The broadband pulse. The left panels show the pressure wave images reconstructed from the phase contrast images with the images in (B)–(E) expanded. The images are recorded approximately 25 mm from the surface of each transducer. The plots on the right show the pressure vs time curves measured with the hydrophone and phase contrast methods. These curves are measured at the locations (1, 2, and 3) indicated by the pink bars and numbers in (A), left. The thicknesses of the curves represent the measurement uncertainty. In all of the images, the lengths of the pink bars represent the 1 mm diameter hydrophone aperture and serve as 1 mm scale bars for the images. The lower pressure amplitude measured in (A) (see curves for locations 2 and 3) is due to the relatively weak efficiency of the 5 MHz transducer when driven at 2 MHz. In (E), the frequency spectrum of the broadband pulse along the transducer AOS, as measured with both methods, is shown to the far right.

hydrophone aperture's geometric diameter.[18,52] The speed of sound is used to convert the z coordinate of the reconstruction into a time coordinate [see the coordinate definitions in Fig. 1(A)]. This space-to-time coordinate conversion is possible because when traversing the field of view, the planar pressure waves do not change shape and are not significantly attenuated. As expected from the information supplied by the transducer manufacturers, the pressure amplitude is largest along the AOS of the transducer.

The phase contrast imaging measurement (blue) and hydrophone method (black) show excellent agreement as seen in the overlaid pressure vs time curves in Fig. 2. To overlay the curves, no fitting parameters are used except a constant time offset to align the curves in time. The thickness of each curve represents its uncertainty. The plotted uncertainty in the hydrophone measurements accounts for the calibration uncertainty (types A and B), whereas the plotted uncertainty in the phase contrast measurements accounts for the uncertainty in C_P (type B), and the variation of six repeated measurements (type A) in which the delay time between the ultrasonic and laser pulses is varied by up to 1.5 μs. Along the AOS (i.e., location 3), the two measurements agree well at all frequencies, but note that toward the edge of the field of view (i.e., location 1), for the 20 MHz tone burst, the phase contrast method measures a lower pressure amplitude modulation and shows a slightly different waveform shape at the start and end of the tone burst. The differences in the waveform amplitude and shape at this high frequency likely result from the emergence of optical diffraction effects as discussed below. Despite these differences, the two methods measure the same ultrasonic frequencies for all of the measured tone bursts. This agreement is confirmed in the curves from the broadband pulse measurements. The two frequency spectra recorded at the same location along the transducer AOS [Fig. 2(E), far right] agree well up to 20 MHz.

Next, sinusoidal ultrasonic tone bursts generated from focused ultrasonic transducers are examined and compared to hydrophone measurements at different locations, 3 mm and 9 mm, beyond the focal point of the transducer (Fig. 3). Measurements are made both on the AOS (on-AOS) and off the AOS (off-AOS) of the transducer with the hydrophone kept in the y-z plane and oriented normal to the local ultrasonic wavefronts. The orientation and position of the hydrophone aperture is verified by recording an image of it with the phase contrast camera. To acquire the pressure vs time curves from the imaging method, the z-coordinate cannot be converted into a time axis as with the flat transducers because the curved wavefronts propagate and expand radially. Instead, the delay time between the ultrasonic and laser pulses is incrementally varied. For each delay time, the average pressure across the hydrophone's geometric aperture is calculated, thereby generating a pressure vs time curve that mimics the hydrophone's spatially averaged response (again, assuming the effective aperture is the geometric aperture).

For the 2 MHz tone burst, the pressure vs time waveforms obtained from each method at 3 mm beyond the

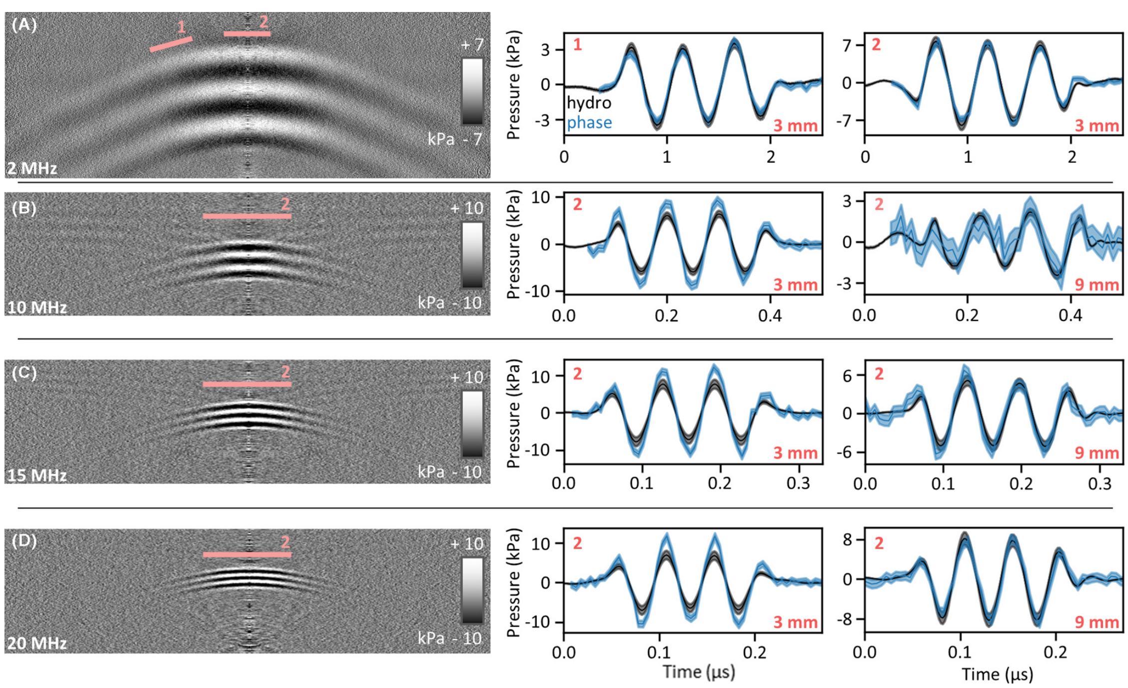

FIG. 3. (Color online) Spherically expanding pressure fields generated from focused ultrasonic transducers. [(A)–(D)] 2 MHz, 10 MHz, 15 MHz, and 20 MHz tone bursts. The left panels show the pressure wave images reconstructed from the phase contrast images recorded 3 mm beyond the ultrasonic focal point with the images in (B)–(D) expanded. In all of the parts, the pink bars serve as 1 mm scale bars, which represent the diameter of the hydrophone's aperture and serve as 1 mm scale bars for the images. The plots to the right show the pressure vs time curves measured with the hydrophone and phase contrast methods. The thicknesses of the curves represent the measurement uncertainty. In (A), these curves are measured 3 mm beyond the ultrasonic focal point at the locations (1 and 2) indicated by the pink bars and numbers in (A), left. In (B)–(D), the pressure vs time curves are measured along the transducer's AOS, 3 mm (leftmost plots) and 9 mm (rightmost plots) beyond the focal point.

ultrasonic focal point agree well regardless of whether the waveform is on-AOS or off-AOS (top two plots in Fig. 3). However, the overlaid waveforms for the 10 MHz tone burst show differences at the 3 mm on-AOS location and the differences increase with frequency [left plots in Figs. 3(B)–3(D)]. On the other hand, the waveforms agree well at the on-AOS location further away (9 mm) from the focal point [right plots in Figs. 3(B)–3(D)]. The increased noise in the phase contrast curve in the rightmost panel of Fig. 3(B) is due to a dust particle in the water bath, which drifts near the ultrasonic field. The plotted uncertainty in the curves for the hydrophone measurements accounts for the calibration uncertainty (types A and B), whereas the plotted uncertainty in the phase measurements accounts for the uncertainty in C_P (type B) and the background shot noise level in the reconstructed pressure distributions (type B).

Based on the series of measurements described above, the frequency of the tone burst and measurement location are found to be key experimental parameters that affect the agreement between the two methods. Note that measurement differences are not noticeable in flat transducers, except for the 20 MHz tone bursts obtained at the far off-AOS location [Fig. 2(D), leftmost plot]. However, more noticeable differences are observed with focused transducers at frequencies of 10 MHz and higher when the measurement point is 3 mm beyond the focal point [Figs. 3(B)–3(D), center]. Figure 4 summarizes the differences between the measurements made with the phase contrast and hydrophone methods. To quantify the difference as a function of the frequency and measurement location, the ratio, $(\beta_c - \beta_h)/\beta_h$, is calculated where β_c and β_h are the spectral amplitudes at the fundamental frequencies of the tone burst as measured by the phase contrast and hydrophone measurements, respectively. Figure 4(A) displays the calculated measurement difference vs frequency for flat transducers, obtained for on-AOS (location 3 in Fig. 2) and off-AOS (location 1 in Fig. 2) locations 25 mm away from the transducer surface. Figure 4(B) displays the measurement differences for focused transducers at two different on-AOS locations, 3 mm and 9 mm beyond the ultrasonic focal point. For each type of transducer, the results are compared at these locations because these locations show the most significant variation in the measurement differences.

For flat transducers [Fig. 4(A)] at both locations, the measurement differences are consistent with zero, verifying that the results of the phase contrast and hydrophone methods agree well. At the off-AOS location (i.e., at the edge of the field of view), the phase contrast method measures a somewhat lower amplitude at high frequencies, resulting in slightly negative difference values. The measurement differences at the on-AOS location are averaged from two repeated measurements and at the off-AOS location, four repeated measurements are averaged. The plotted uncertainty accounts for the uncertainty in the hydrophone calibration (types A and B), the uncertainty in C_P (type B), and the variation of the difference from the repeated measurements (type A). The uncertainty in the difference

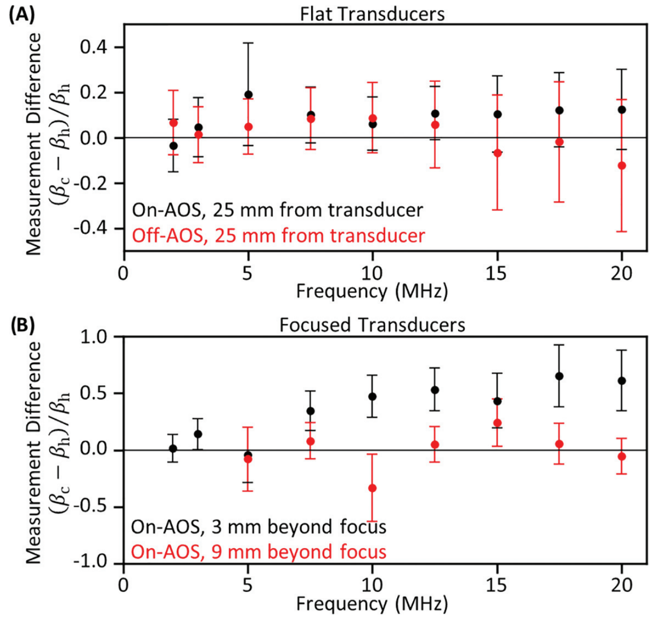

FIG. 4. The differences between the optical and hydrophone measurements. β_c and β_h are the spectral amplitudes at the fundamental frequencies of the ultrasonic tone bursts as measured by the phase contrast and hydrophone measurements, respectively. (A) The measurement difference as a function of the frequency for planar wavefronts on and off the AOS [positions 1 and 3 in Fig. 2(A)]. On-AOS, the total uncertainty in the measurement difference increases from 12% at 2 MHz to 18% at 20 MHz, and off-AOS it increases from 14% to 29%. (B) The measurement difference as a function of the frequency along the AOS of curved wavefronts 3 mm and 9 mm beyond the focus of the transducer. Note the different vertical scales in (A) and (B).

measurement becomes larger at the edge of the field of view at high frequencies. This increasing uncertainty is due to a larger variation in the measured values with repeated phase contrast measurements and, thus, reflects a decreasing accuracy away from the AOS. At 2 MHz, the uncertainty contribution due to the phase contrast measurements is 4% on-AOS and 8% off-AOS, whereas at 20 MHz, it is 18% on-AOS and 24% off-AOS.

Figure 4(B) shows the difference between the two methods as a function of frequency for curved wavefronts generated from focused transducers as measured along the transducers' AOS at 3 mm and 9 mm beyond the transducers' focus. The plotted uncertainty accounts for the uncertainty in the hydrophone calibration (types A and B), the uncertainty in C_P (type B), and shot noise in the image (type B). Close to the focus, the hydrophone method measures a significantly smaller amplitude at high frequencies, resulting in a large positive measurement difference. This difference is likely due to the near field effect. The near field effect can reduce the accuracy of the hydrophone measurements when the distance between the focus and hydrophone approaches the near field distance, $d = D^2 f/4c$, where D is the diameter of the hydrophone's active element.[53] This effect arises because the curved shape of ultrasonic wavefront does not match the flat shape of the hydrophone's active element. Indeed, by inspection of Figs. 3(B)–3(D), left, it is clear that the ultrasonic wavefront amplitude, direction, and phase vary significantly across the 1 mm active element. For the 1 mm diameter hydrophone at 20 MHz, the near field distance is 3.3 mm, therefore, the hydrophone measurements are expected to be affected at high frequencies at the 3 mm measurement distance. Because the near field distance decreases quadratically with D, a hydrophone with a smaller active element (for example, with $D = 0.2$ mm) would likely not suffer from this effect. The sensitivity of hydrophones also decreases roughly quadratically with D, so measurements with a smaller active element hydrophone would have a significantly lower signal-to-noise ratio.

Because the phase contrast and hydrophone measurements are compared by averaging the phase contrast measurement across the hydrophone aperture, the two methods are expected to agree if the spatial averaging effect fully describes the hydrophone's response.[5,17,18] The significant difference between the measurements at the location 3 mm beyond the focal point [Fig. 4(B), up to 60%] suggests that other effects are important. Previous work has also found that spatial averaging does not fully account for the hydrophone response when measuring focused ultrasonic fields in which the hydrophone element diameter is comparable to or larger than the width of the focused ultrasonic field.[54,55] For example, Martin and Treeby[54] found a 20% difference in the measured pressure amplitude after accounting for spatial averaging effects when using a hydrophone with a 0.4 mm diameter hydrophone to measure a 3.3 MHz, 0.6 mm diameter focused ultrasonic field. They found that the measurement difference increases with the ultrasonic frequency and when the hydrophone active element diameter increases relative to the diameter of the ultrasonic field. In comparison to these results, the 60% measurement difference in Fig. 4(B) is not unexpected given that a hydrophone with a 1 mm diameter aperture is used to measure the focused ultrasonic fields with frequencies up to 20 MHz and beam diameters as small as 0.7 mm. Investigating the reasons behind the observed differences may be the subject of future work.

Previous investigations of the optical imaging methods have shown close quantitative agreement for frequencies of 2.5 MHz or lower.[25,28,30,37] These studies did not attempt to measure higher frequency ultrasonic fields, but because they measured ultrasonic fields with extents of $L \gtrsim 10$ mm and used optical wavelengths $\lambda \geq 532$ nm,[25,28,30,37] if they applied the same measurement setups at 20 MHz frequencies, the Klein-Cook parameter [Eq. (2)] would be $Q \gtrsim 4.5$ and significant optical diffraction would be expected.[41,42] The present implementation extends optical imaging to higher ultrasonic frequencies by tailoring the experimental conditions ($L \leq 6$ mm, $\lambda = 470$ nm) to minimize the diffraction effects. The largest measured Raman-Nath parameter (largest measured phase shift) is $\nu = 0.05$, and the largest value of the Klein-Cook parameter is $Q = 2.4$ [Eq. (2)], which occurs for the 20 MHz planar tone bursts ($L = 6$ mm). Because the Klein-Cook parameter exceeds two at the highest frequencies measured, the decreasing accuracy at the edge of the field of view at 20 MHz [Fig. 2(D), leftmost plot] is likely to the result of the emerging diffraction effects. The phase contrast method is expected to remain accurate at frequencies above 20 MHz only if the optical wavelength and/or ultrasonic field's extent are reduced to keep the Klein-Cook parameter smaller than two. The observed measurement differences for focused ultrasonic waves at the measurement point 3 mm beyond the focus [Fig. 4(B)] are unlikely caused by optical diffraction. In this case, the small extent of the ultrasonic field ($L \approx 1$ mm) keeps the Klein-Cook parameter below 0.4.

The findings in the present paper are consistent with the results of a non-imaging, point-based optical detection method, which was also demonstrated at high ultrasonic frequencies but only with continuous sinusoidal, planar ultrasonic fields.[56–58] This non-imaging method also underestimates the ultrasonic pressure amplitude when the Klein-Cook parameter exceeds two.[56] Indeed, one such measurement at a frequency of 13.85 MHz measured a pressure 20% smaller than that measured with a calibrated hydrophone with the large Klein-Cook parameter ($Q = 6$) being the reason for the measurement difference.[57] Another measurement showed excellent agreement with a calibrated hydrophone at 20.18 MHz ($Q = 13$).[58] In this study, the authors overcame diffraction effects by orienting the illumination at a specific angle of incidence (the Bragg angle) to the ultrasonic wavefronts. This implies the limitation of $Q \leq 2$ might be relaxed for the phase contrast approach if the ultrasonic wavefronts happen to be planar and Bragg incidence is used.

The present study also suggests that the Klein-Cook parameter is a key metric to consider when using the phase contrast measurement approach for imaging applications. For example, Nuster, Paltauf, and co-workers[21,22,59] previously demonstrated that a phase contrast approach can measure photoacoustically generated ultrasonic fields, and these measurements can be used to reconstruct high-resolution images of the samples. They report relative measurements of ultrasonic pressures at frequencies up to 23 MHz. At this high frequency, for their apparatus (20 mm wide ultrasonic field, 530 nm illumination), the Klein-Cook parameter is $Q = 12$. Thus, diffraction effects may degrade their reconstructed images. Lowering the Klein-Cook parameter (by using shorter wavelength light and imaging the ultrasonic field before it expands to 20 mm) may improve the reconstructed image quality.

IV. CONCLUSION

Optical phase contrast imaging can quantitatively measure the ultrasonic pressure fields with frequencies up to 20 MHz. The method can quickly characterize the ultrasonic fields with complex wavefront shapes such as near field waves. Because the method is compatible with arbitrary wavefront shapes, it is ideally suited to measure ultrasonic fields generated from imaging applications, such as photoacoustic imaging, especially if the method's quantitative accuracy can be extended to even higher ultrasonic frequencies.

The Klein-Cook parameter [Eq. (2)] limits the maximum ultrasonic frequency for accurate measurements by optical imaging methods. Although not explored in the present work, the Raman-Nath parameter likely also limits which ultrasonic fields can be accurately measured. The Raman-Nath parameter does not depend on the ultrasonic frequency, but because it depends on the pressure field's amplitude,[41,42] it will be important to consider when applying optical imaging methods to the ultrasonic fields with pressure amplitudes approaching 100 kPa or higher. Similar to the phase contrast method employed here, other optical imaging methods used to measure ultrasonic fields assume that the diffraction effects are negligible[16,26] and are, thus, also expected to be subject to the same limits on the Klein-Cook and Raman-Nath parameters. Extending optical imaging techniques beyond these limits requires accounting for diffraction effects, which might be achieved with optical diffractive tomography.[60]

Because phase contrast imaging produces absolute pressure measurements, it might also be developed for use as a primary calibration method for hydrophones or transducers. It could be particularly useful for calibrating hydrophones and transducers with nonplanar elements,[23,38,61] which is difficult with current calibration methods.[1,5,12,62,63] However, additional work is needed to fully characterize the measurement uncertainty such as accounting for the effects of aberrations in the images and any imperfections in the Fourier masks. Also, because most calibrated transducers and hydrophones are used at pressure amplitudes in the MPa range,[2] the accuracy of the phase contrast method must be tested at these pressure amplitudes, which are much higher than the roughly 1–10 kPa pressure amplitudes used here.

Finally, optical imaging methods, in principle, can be applied in any optically accessible (transmissive) material. They have been previously demonstrated in transparent solids.[64] This feature of optical ultrasonic detection could eventually enable noninvasive, absolute pressure measurements of high frequency ultrasonic fields in environments inaccessible to calibrated hydrophones such as within ultrasonic[65,66] and photoacoustic[67,68] imaging phantoms with optically transparent layers or compartments.

ACKNOWLEDGMENTS

The authors thank David Plusquellic and Ward Johnson for the loan of equipment and careful readings of the manuscript. The authors also thank two anonymous journal reviewers for their detailed feedback. This research was performed while A.M.G. held a National Research Council (NRC) Research Associateship award as part of the NRC Research Associateship Program of the National Academies of Science, USA. Certain commercial equipment, instruments, or materials are identified in this paper to specify the experimental procedure adequately. Such identification is not intended to imply recommendation or endorsement by the National Institute of Standards and Technology or that the materials or equipment identified are necessarily the best available for the purpose.

[1]C. R. Hill, "Detection and measurement of acoustic fields," in *Physical Principles of Medical Ultrasonics*, 2nd ed., edited by C. R. Hill, J. C. Bamber, and G. R. ter Haar (Wiley, Chichester, West Sussex, England, 2004), pp. 69–91.

[2]IEC 62127-1:2007+AMD1:2013 CSV, *Ultrasonics—Hydrophones—Part 1: Measurement and Characterizationof Medical Ultrasonic Fields up to 40 MHz* (International Electrotechnical Commission, Geneva, Switzerland, 2013).

[3]IEC 62127-3:2007+AMD1:2013 CSV, *Ultrasonics—Hydrophones—Part 3: Properties of Hydrophones for Ultrasonic Fields up to 40 MHz* (International Electrotechnical Commission, Geneva, Switzerland, 2013).

[4]S. Rajagopal, C. R. Fury, B. Zeqiri, M. Brandt, V. Wilkens, C. Koch, Y. Matsuda, M. Yoshioka, Y. Ping, Z. Yan, B. Wenping, R. P. B. Costa-Felix, and E. G. Oliveira, "Report on BIPM/CIPM key comparison CCAUV.U-K4: Absolute calibration of medical hydrophones in the frequency range 0.5 MHz to 20 MHz," Metrologia **53**, 09004 (2016).

[5]IEC 62127-2:2007+AMD1:2013+AMD2:2017 CSV, *Ultrasonics—Hydrophones—Part 2: Calibration for Ultrasonic Fields up to 40 MHz* (International Electrotechnical Commission, Geneva, Switzerland, 2017).

[6]R. A. Smith and D. R. Bacon, "A multiple-frequency hydrophone calibration technique," J. Acoust. Soc. Am. **87**, 2231–2243 (1990).

[7]M. Weber and V. Wilkens, "Using a heterodyne vibrometer in combination with pulse excitation for primary calibration of ultrasonic hydrophones in amplitude and phase," Metrologia **54**, 432–444 (2017).

[8]Y. Matsuda, M. Yoshioka, T. Uchida, and T. Kikuchi, "Absolute calibration of membrane hydrophones up to 40 MHz in ultrasonic far-field," in *2012 IEEE International Ultrasonics Symposium* (2012), pp. 374–377.

[9]P. Yang, G. Xing, and L. He, "Calibration of high-frequency hydrophone up to 40 MHz by heterodyne interferometer," Ultrasonics **54**, 402–407 (2014).

[10]S. Rajagopal, B. Zeqiri, and P. N. Gélat, "Calibration of miniature medical ultrasonic hydrophones for frequencies in the range 100 to 500 kHz using an ultrasonically absorbing waveguide," IEEE Trans. Ultrason. Ferroelectr. Freq. Control **61**, 765–778 (2014).

[11]R. C. Preston, S. P. Robinson, B. Zeqiri, T. J. Esward, P. N. Gélat, and N. D. Lee, "Primary calibration of membrane hydrophones in the frequency range 0.5 MHz to 60 MHz," Metrologia **36**, 331–343 (1999).

[12]T. Koukoulas, S. Robinson, S. Rajagopal, and B. Zeqiri, "A comparison between heterodyne and homodyne interferometry to realise the SI unit of acoustic pressure in water," Metrologia **53**, 891–898 (2016).

[13]E. G. Oliveira, R. P. B. Costa-Felix, and J. C. Machado, "Primary reciprocity-based method for calibration of hydrophone magnitude and phase sensitivity: Complete tests at frequencies from 1 to 7MHz," Ultrasonics **58**, 87–95 (2015).

[14]G. Xing, P. Yang, W. Shou, M. Wang, X. Feng, and L. He, "Hydrophone reciprocity calibration in spherically focused ultrasonic field from 1 MHz to 15 MHz," Acta Acust. Acust. **105**, 273–283 (2019).

[15]K. A. Wear, P. M. Gammell, S. Maruvada, Y. Liu, and G. R. Harris, "Time-delay spectrometry measurement of magnitude and phase of hydrophone response," IEEE Trans. Ultrason. Ferroelectr. Freq. Control **58**, 2325–2333 (2011).

[16]G. Wissmeyer, M. A. Pleitez, A. Rosenthal, and V. Ntziachristos, "Looking at sound: Optoacoustics with all-optical ultrasound detection," Light Sci. Appl. **7**, 53 (2018).

[17]K. A. Wear and S. M. Howard, "Correction for spatial averaging artifacts in hydrophone measurements of high-intensity therapeutic ultrasound: An inverse filter approach," IEEE Trans. Ultrason. Ferroelectr. Freq. Control **66**, 1453–1464 (2019).

[18]K. A. Wear, "Considerations for choosing sensitive element size for needle and fiber-optic hydrophones—Part I: Spatiotemporal transfer function and graphical guide," IEEE Trans. Ultrason. Ferroelectr. Freq. Control **66**, 318–339 (2019).

[19]B. Zeqiri and A. D. Bond, "The influence of waveform distortion on hydrophone spatial-averaging corrections—Theory and measurement," J. Acoust. Soc. Am. **92**, 1809–1821 (1992).

[20]M. P. Cooling, V. F. Humphrey, and V. Wilkens, "Hydrophone area-averaging correction factors in nonlinearly generated ultrasonic beams," J. Phys.: Conf. Ser. **279**, 012002 (2011).
[21]R. Nuster, P. Slezak, and G. Paltauf, "High resolution three-dimensional photoacoustic tomography with CCD-camera based ultrasound detection," Biomed. Opt. Express **5**, 2635–2647 (2014).
[22]R. Nuster and G. Paltauf, "Comparison of piezoelectric and optical projection imaging for three-dimensional *in vivo* photoacoustic tomography," J. Imag. **5**, 15 (2019).
[23]J. Yao and L. V. Wang, "Photoacoustic microscopy," Laser Photonics Rev. **7**, 758–778 (2013).
[24]B. Dong, C. Sun, and H. F. Zhang, "Optical detection of ultrasound in photoacoustic imaging," IEEE. Trans. Biomed. Eng. **64**, 4–15 (2017).
[25]T. Nakamura, R. Iwasaki, S. Yoshizawa, and S. Umemura, "Quantitative measurement of ultrasonic pressure field using combination of optical phase contrast and nonlinear acoustic holography methods," Jpn. J. Appl. Phys. **57**, 07LB13 (2018).
[26]N. Kudo, "Optical methods for visualization of ultrasound fields," Jpn. J. Appl. Phys. **54**, 07HA01 (2015).
[27]A. Pulkkinen, J. J. Leskinen, and A. Tiihonen, "Ultrasound field characterization using synthetic schlieren tomography," J. Acoust. Soc. Am. **141**, 4600–4609 (2017).
[28]H. Hanayama, T. Nakamura, R. Takagi, S. Yoshizawa, and S. Umemura, "Simulation of optical propagation based on wave optics for phase retrieval in shadowgraph of ultrasonic field," Jpn. J. Appl. Phys. **56**, 07JC13 (2017).
[29]L. Chen, S. J. Rupitsch, and R. Lerch, "A reliability study of light refractive tomography utilized for noninvasive measurement of ultrasound pressure fields," IEEE Trans. Ultrason. Ferroelectr. Freq. Control **59**, 915–927 (2012).
[30]T. A. Pitts, A. Sagers, and J. F. Greenleaf, "Optical phase contrast measurement of ultrasonic fields," IEEE Trans. Ultrason. Ferroelectr. Freq. Control **48**, 1686–1694 (2001).
[31]H. Li, B. Dong, Z. Zhang, H. F. Zhang, and C. Sun, "A transparent broadband ultrasonic detector based on an optical micro-ring resonator for photoacoustic microscopy," Sci. Rep. **4**, 4496 (2014).
[32]E. Zhang, J. Laufer, and P. Beard, "Backward-mode multiwavelength photoacoustic scanner using a planar Fabry-Perot polymer film ultrasound sensor for high-resolution three-dimensional imaging of biological tissues," Appl. Opt. **47**, 561–577 (2008).
[33]A. Rosenthal, D. Razansky, and V. Ntziachristos, "High-sensitivity compact ultrasonic detector based on a pi-phase-shifted fiber Bragg grating," Opt. Lett. **36**, 1833–1835 (2011).
[34]G. Rousseau, B. Gauthier, A. Blouin, and J.-P. Monchalin, "Non-contact biomedical photoacoustic and ultrasound imaging," J. Biomed. Opt. **17**, 061217 (2012).
[35]X. Zhu, Z. Huang, G. Wang, W. Li, D. Zou, and C. Li, "Ultrasonic detection based on polarization-dependent optical reflection," Opt. Lett. **42**, 439–441 (2017).
[36]R. Haupt, C. Wynn, B. Anthony, J. Fincke, A. Samir, and X. Zhang, "Non-contact laser ultrasound concept for biomedical imaging," *2017 IEEE International Ultrasonics Symposium (IUS)* (2017), pp. 1–5.
[37]T. A. Pitts and J. F. Greenleaf, "Fresnel transform phase retrieval from magnitude," IEEE Trans. Ultrason. Ferroelectr. Freq. Control **50**, 1035–1045 (2003).
[38]S. Harigane, R. Miyasaka, S. Yoshizawa, and S. Umemura, "Optical phase contrast mapping of highly focused ultrasonic fields," Jpn. J. Appl. Phys. **52**, 07HF07 (2013).
[39]C. I. Zanelli and S. M. Howard, "Schlieren metrology for high frequency medical ultrasound," Ultrasonics **44**, e105–e107 (2006).
[40]S. Oyama, J. Yasuda, H. Hanayama, S. Yoshizawa, and S. Umemura, "Quantitative measurement of ultrasound pressure field by optical phase contrast method and acoustic holography," Jpn. J. Appl. Phys. **55**, 07KB09 (2016).
[41]W. R. Klein and B. D. Cook, "Unified approach to ultrasonic light diffraction," IEEE Trans. Ultrason. Ferroelectr. Freq. Control **14**, 123–134 (1967).
[42]R. Reibold and P. Kwiek, "On ultrasound light diffraction," Ultrasonics **31**, 307–313 (1993).
[43]Y.-K. Zhu, G.-Y. Tian, R.-S. Lu, and H. Zhang, "A review of optical NDT technologies," Sensors **11**, 7773–7798 (2011).
[44]S.-L. Chen, "Review of laser-generated ultrasound transmitters and their applications to all-optical ultrasound transducers and imaging," Appl. Sci. **7**, 25 (2017).
[45]L. V. Wang and J. Yao, "A practical guide to photoacoustic tomography in the life sciences," Nat. Methods **13**, 627–638 (2016).
[46]L. Weiss, A. Tazibt, A. Tidu, and M. Aillerie, "Water density and polarizability deduced from the refractive index determined by interferometric measurements up to 250 MPa," J. Chem. Phys. **136**, 124201 (2012).
[47]J. W. Goodman, *Introduction to Fourier Optics*, 3rd ed. (Roberts and Company, Englewood, CO, 2005).
[48]N. H. Abel, "Auflösen einer mechanischen Aufgabe" ("Solving a mechanical task"), J. Reine Angew. Math. **1**, 153–157 (1826).
[49]S. Gibson, D. D. Hickstein, R. Yurchak, M. Ryazanov, D. Das, and G. Shih, "PyAbel/PyAbel (version 0.8.3) [computer program]," Zenodo (2019), https://zenodo.org/record/3370021#.YNEnYW5MHUY (Last viewed 21 June 2021).
[50]V. Dribinski, A. Ossadtchi, V. A. Mandelshtam, and H. Reisler, "Reconstruction of Abel-transformable images: The Gaussian basis-set expansion Abel transform method," Rev. Sci. Instrum. **73**, 2634–2642 (2002).
[51]L. S. Shraiber, "Experimental investigation of the thermal dependence of the piezo-optical coefficient of water between 5 and 90 °C," Isr. J. Chem. **13**, 181–184 (1975).
[52]K. A. Wear, C. Baker, and P. Miloro, "Directivity and frequency-dependent effective sensitive element size of needle hydrophones: Predictions from four theoretical forms compared with measurements," IEEE Trans. Ultrason. Ferroelectr. Freq. Control **65**, 1781–1788 (2018).
[53]J. Krautkrämer and H. Krautkrämer, *Ultrasonic Testing of Materials*, 3rd ed. (Springer, Berlin, 1983).
[54]E. Martin and B. Treeby, "Investigation of the repeatability and reproducibility of hydrophone measurements of medical ultrasound fields," J. Acoust. Soc. Am. **145**, 1270–1282 (2019).
[55]Y. Liu, K. A. Wear, and G. R. Harris, "Variation of high-intensity therapeutic ultrasound (HITU) pressure field characterization: Effects of hydrophone choice, nonlinearity, spatial averaging and complex deconvolution," Ultrasound Med. Biol. **43**, 2329–2342 (2017).
[56]R. Reibold and P. Kwiek, "Uncertainty considerations of ultrasonic field mapping by light-diffraction tomography," Ultrasonics **35**, 187–193 (1997).
[57]P. Kwiek, W. Molkenstruck, and R. Reibold, "Optical mapping of ultrasonic fields in the intermediate range between weak and strong acousto-optical interaction," Ultrasonics **35**, 499–507 (1997).
[58]P. Kwiek, W. Molkenstruck, and R. Reibold, "Optical mapping of ultrasonic fields using Bragg incidence," Ultrasonics **36**, 775–781 (1998).
[59]R. Nuster, G. Zangerl, M. Haltmeier, and G. Paltauf, "Full field detection in photoacoustic tomography," Opt. Express **18**, 6288–6299 (2010).
[60]D. Jin, R. Zhou, Z. Yaqoob, and P. T. C. So, "Tomographic phase microscopy: Principles and applications in bioimaging," J. Opt. Soc. Am. B **34**, B64–B77 (2017).
[61]D.-K. Yao, K. Maslov, K. K. Shung, Q. Zhou, and L. V. Wang, "*In vivo* label-free photoacoustic microscopy of cell nuclei by excitation of DNA and RNA," Opt. Lett. **35**, 4139–4141 (2010).
[62]J. Civale, I. Rivens, A. Shaw, and G. ter Haar, "Focused ultrasound transducer spatial peak intensity estimation: A comparison of methods," Phys. Med. Biol. **63**, 055015 (2018).
[63]Y. Wang, M. Sun, Y. Cao, and J. Zhu, "Application of optical interferometry in focused acoustic field measurement," J. Sound Vib. **426**, 234–243 (2018).
[64]L. Chen, S. J. Rupitsch, J. Grabinger, and R. Lerch, "Quantitative reconstruction of ultrasound fields in optically transparent isotropic solids," IEEE Trans. Ultrason. Ferroelectr. Freq. Control **61**, 685–695 (2014).
[65]M.-K. Sun, J. Shieh, C.-W. Lo, C.-S. Chen, B.-T. Chen, C.-W. Huang, and W.-S. Chen, "Reusable tissue-mimicking hydrogel phantoms for focused ultrasound ablation," Ultrason. Sonochem. **23**, 399–405 (2015).
[66]A. I. Chen, M. L. Balter, M. I. Chen, D. Gross, S. K. Alam, T. J. Maguire, and M. L. Yarmush, "Multilayered tissue mimicking skin and vessel phantoms with tunable mechanical, optical, and acoustic properties," Med. Phys. **43**, 3117–3131 (2016).
[67]W. C. Vogt, C. Jia, K. A. Wear, B. S. Garra, and T. J. Pfefer, "Biologically relevant photoacoustic imaging phantoms with tunable optical and acoustic properties," J. Biomed. Opt. **21**, 101405 (2016).
[68]E. Maneas, W. Xia, O. Ogunlade, M. Fonseca, D. I. Nikitichev, A. L. David, S. J. West, S. Ourselin, J. C. Hebden, T. Vercauteren, and A. E. Desjardins, "Gel wax-based tissue-mimicking phantoms for multispectral photoacoustic imaging," Biomed. Opt. Express **9**, 1151–1163 (2018).